Numerical analysis of an injection-locked gyrotron backward-wave oscillator with tapered sections

A. Grudiev* and K. Schünemann

Institut für Hochfrequenztechnik, Technische Universität Hamburg-Harburg, D-21071 Hamburg, Germany
(Received 15 February 2003; published 9 July 2003)

Injection-locked operation of a gyrotron backward-wave oscillator (gyro-BWO) is investigated by means of our time-dependent self-consistent code. Numerical results for a 100 kW, Ka-band, TE_{11}-mode gyro-BWO developed at NTHU, Hsinchu, Taiwan, are compared to the experimental ones. The results are in good agreement showing, in both cases, the asymmetric form of the locking bandwidth curve. Comparison of these results obtained for the case of injection of the external signal into the upstream port, as has been done in the experiments, to the results for injection into the downstream port is made. The results of the comparison demonstrate that the asymmetry of the locking bandwidth curves must be attributed to the influence of the injection signal on the electron bunching that takes place in the input tapered section. Moreover, in some cases, this influence results also in a significant increase of the locking bandwidth (up to a factor of 5). An increase of the output power of the locked gyro-BWO over the output power of the free running one is also investigated and compared with the experimental data.

I. INTRODUCTION

Since the mid-1960s, when the first studies on the theory of a gyrotron backward-wave oscillator (gyro-BWO) have appeared in the Soviet literature (see Ref. [1] reviewing the studies), both theoretical (see Refs. [1–15]) and experimental (see Refs. [16–25]) investigations of gyro-BWOs have been motivated by their potential applications as tunable millimeter-wave sources including position selective heating of fusion plasma, deep space communications, high resolution radars, spectroscopy, materials processing, and drivers of ultrahigh power amplifiers. These applications exploit the main advantage of gyro-BWOs over gyromonotrons, namely, that the operating frequency can be continuously tuned over a wide range by changing the applied magnetic field or the beam voltage. This is possible because a feedback loop, which is formed by the interaction between the forward moving beam of electrons gyrating in the applied magnetic field and the oppositely propagating electromagnetic wave, allows a nonresonant structure to be employed. Both magnetic and voltage tunability have been successfully demonstrated in the experiments, as is reported in Ref. [16] and in Refs. [16,18,20], respectively. The disadvantage of gyro-BWOs is the lower efficiency compared to gyromonotrons. One reason for this is an unfavorable axial structure of the electromagnetic field. Another one is the impossibility to set an optimal mismatch between the wave frequency and the Doppler-down-shifted cyclotron frequency in order to yield maximal efficiency (see Ref. [9]). Both uptapering the applied magnetic field (see Refs. [1,5,8,16,21]) and downtapering the waveguide radius (see Refs. [1,11,19,21]) have been shown to be effective means for efficiency enhancement. On the other hand, there are issues of physical interest as well as practical importance that remains to be addressed, such as the spectral purity, the phase and frequency controllability, and the stability of tuning.

Controlling the phase and frequency in oscillators by means of locking, as described in Ref. [26], has been known for decades (see also Ref. [27] Chap. 1, for a historical survey). This approach has also been applied to both gyromonotrons and gyro-BWOs, however, with a different degree of activity. Although injection-locked operation of gyromonotrons has been investigated both theoretically (see Refs. [28–33]) and experimentally (see Refs. [34–36]) by several teams, only one team from Taiwan has done several experiments on injection-locked gyro-BWOs presented in Refs. [18,24]. In Ref. [18], the spectral purity and phase of the gyro-BWO output signal have been controlled by means of injection-locking techniques. Moreover, in a recent work described in Ref. [24], injection-locking of a Ka-band gyro-BWO has resulted in an output power of 154 kW, a significant enhancement over the free running power of 100 kW. These very interesting and promising experimental results still call for a theoretical explanation. To the best of our knowledge, up to now, no work on the theory of injection-locked gyro-BWOs has been published.

In this work, we try to gain insight into the operation of injection-locked gyro-BWOs with tapered input and output sections, which have been investigated in the experiments reported in Refs. [18,24]. Our self-consistent time-dependent analysis, which has already been used to study nonstationary behavior of such gyro-BWOs, as presented in Ref. [14], is utilized. In Sec. II, this analysis and its modifications for introducing an injection signal are presented. In Sec. III, the obtained numerical results are shown, discussed, and compared with experimental results.

II. THEORY

A. Modeling free-running gyro-BWO

In this work, we utilize our self-consistent time-dependent code for gyro-device simulation, which was recently developed. Without going into details of the derivation given in

---

*Present address: CERN, AB-RF, CH–1211 Geneva 23, Switzerland.

Refs. [37,38], let us point out the distinctive features of our approach. An accurate representation of the electromagnetic field is obtained by expanding the field components in terms of the eigenfunctions of the equivalent completely closed cavity. The eigenfunctions satisfy the short-circuit boundary condition on the metallic walls and the open-circuit boundary condition at the aperture surfaces, which allows us to satisfy zero electric field on the metallic walls if we neglect the ohmic losses, and to improve the convergence of the electric field in the vicinity of the apertures with respect to the chosen number of eigenfunctions. The use of the eigenfunction expansion method reduces the boundary value problem for the field components associated with the solution of Maxwell's equations to that of solving a linear system of ordinary differential equations (ODE) for the expansion coefficients. Replacing the nonvanishing tangential magnetic field at the apertures by an equivalent surface electric current allows to model the power propagation through the aperture surface according to the equivalence principle described in Ref. [39]. Moreover, by taking a characteristic admittance relation between the electric and magnetic fields of a waveguide mode and by applying this relation to the electric and magnetic fields at the aperture, we can satisfy the outgoing wave boundary condition at any frequency higher than the cutoff frequency of the aperture cross section. Furthermore, a convolution technique along with analytic expressions for the characteristic admittances of the waveguide modes in time domain are applied to accurately formulate the time-dependent outgoing wave boundary condition at the apertures.

Although our approach is not restricted to only one mode, in this work, we assume that only the fundamental TE_{11} circular waveguide mode is present in the device. Moreover, space-charge effects are neglected. Hence, the equations derived in Refs. [37,38] can be written as

$$\boldsymbol{E} = \sum_n A_n \mathbf{E}_n, \tag{1a}$$

$$\boldsymbol{H} = \sum_n C_n \mathbf{H}_n, \tag{1b}$$

where the orthonormal electric $\{\mathbf{E}_n\}$ and magnetic $\{\mathbf{H}_n\}$ solenoidal eigenfunctions are used to describe the spatial structure of the vector fields, and the expansion coefficients $\{A_n; C_n\}$ are time-dependent and must be found from the following system of equations:

$$\frac{1}{Z_0 c}\frac{d}{dt}A_n - k_n C_n = -\tilde{A}_n - [K_{nm}]I_m, \tag{2a}$$

$$\frac{Z_0}{c}\frac{d}{dt}C_n + k_n A_n = 0, \tag{2b}$$

$$I_m = [Y] * V_m, \tag{3}$$

$$V_m = \tfrac{1}{2}([U]-[S])*([K_{nm}]^{\mathrm{T}} a_n), \tag{4}$$

$$\frac{1}{Z_0 c}\frac{d}{dt}a_n - k_n c_n = -\tilde{A}_n, \tag{5a}$$

$$\frac{Z_0}{c}\frac{d}{dt}c_n + k_n a_n = 0, \tag{5b}$$

where Z_0 denotes wave impedance of vacuum, c is the velocity of light in vacuum, and $[K_{nm}]$ is the matrix of the constant coupling coefficients (see Ref. [37] for details). V_m and I_m mean amplitudes of the electric and magnetic field (or equivalent voltages and currents) of the working eigenmode at the apertures, respectively. $m=1,2$ counts the apertures. The matrices $[U]$, $[S]$, and $[Y]$ are square matrices of dimension 2×2, whose time-dependent elements result from an element-to-element inverse Laplace transform of the unity matrix, the scattering matrix of the structure, and the matrix of the wave admittances of the working eigenmode at the apertures, respectively (see Ref. [38] for details). In Eqs. (3) and (4) $*$ means a convolution between a matrix and a vector with time-dependent elements. The volume current expansion coefficients $\{\tilde{A}_n\}$ are expressed as

$$\tilde{A}_n = \int \int \int_V \boldsymbol{J} \cdot \mathbf{E}_n \, dV \tag{6}$$

for a given volume current density distribution $\boldsymbol{J}$. The presented formulation is valid for describing a field of arbitrary time dependence showing a broad frequency spectrum.

The electron beam is represented by an ensemble of particles defining the volume current density $\boldsymbol{J}$ according to

$$\boldsymbol{J} = \sum_j \boldsymbol{v}_j q_j \delta(\boldsymbol{r} - \boldsymbol{r}_j), \tag{7}$$

where the charge distribution of a single particle is a Dirac $\delta(\boldsymbol{r})$ function and q_j denotes its charge. For each particle, the relativistic equation of motion

$$\frac{d}{dt}\boldsymbol{p}_j = q_j[\boldsymbol{E} + \boldsymbol{v}_j \times (\mathbf{B}_0 + \mu_0 \boldsymbol{H})], \tag{8a}$$

$$\frac{d}{dt}\boldsymbol{r}_j = \boldsymbol{v}_j \quad \text{with} \quad \boldsymbol{v}_j = \frac{\boldsymbol{p}_j}{\gamma_j m_j} \tag{8b}$$

must be solved, where $\mathbf{B}_0$ means magnetic induction in the cavity, and m_j and γ_j are mass and relativistic factor of the jth particle, respectively. The resulting system of time-dependent equations (1)–(8) has been successfully used to study the nonstationary behavior of gyro-BWOs (see Ref. [14]). This system must be completeded here by encompassing an injection signal.

B. Introducing an injection signal into the system

Consider now injection signals in the connecting waveguides. Then in- and outgoing traveling waves superpose to V_m and I_m according to

$$V_m = V_m^+ + V_m^-, \tag{9a}$$

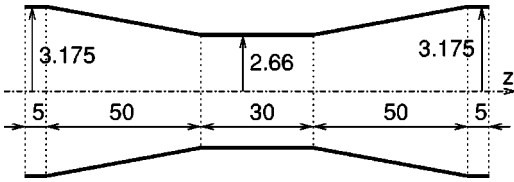$$I_m = I_m^+ - I_m^-, \tag{9b}$$

FIG. 1. Geometry of the interaction structure. All dimensions are in mm.

where the superscript $^+$ means an outgoing and $^-$ means an ingoing wave. The latter represents an injection signal, so that V_m^- can be assumed to be given as

$$V_m^- = V_{inj}\sin(\omega_{inj}t),\qquad(10)$$

where m is equal to 1 or 2 depending on whether the upstream or the downstream port is used for injection, $\omega_{inj}=2\pi f_{inj}$ denotes injection frequency, $V_{inj}=[2P_{inj}/Y_m(\omega_{inj})]^{1/2}$ means amplitude of equivalent voltage of injection signal, P_{inj} denotes injection power, and Y_m means the characteristic admittance at the aperture of the mth port.

Reformulating Eqs. (2)–(5) by invoking Eqs. (9) leads to a similar system, where only Eq. (4) is replaced by

$$V_m^+ = V_m^- + \tfrac{1}{2}([U]-[S])*([K_{nm}]^T a_n - 2V_m^-).\qquad(11)$$

Then Eqs. (1)–(3), (5)–(9a), (10), and (11) form the complete system of equations describing a gyro-BWO operating in the presence of an injection signal. This system is solved self-consistently using a semi-implicit multistep integration scheme described in Ref. [38].

III. NUMERICAL RESULTS AND DISCUSSIONS

A. Gyro-BWO interaction structure

The interaction structure which has been used in the experiments on an injection-locked gyro-BWO reported in Ref. [24] is used in the simulation. Its geometry is presented in Fig. 1 showing a uniform interaction section connected at both ends by weakly tapered sections to short uniform sections of larger radius. gyro-BWOs with similar interaction structure have been investigated both numerically (see Refs. [12–14]) and experimentally (see Refs. [18,24,25]). The influence of the downtapered input section on the gyro-BWO behavior has been emphasized in Ref. [13]. Moreover, in the simulations described in Refs. [13,14] as well as in the experiments presented in Ref. [25], two regimes of operation have been observed: the gyro-BWO regime, where an electron beam interacts with a counterpropagating electromagnetic wave, and the gyromonotron regime, where an electron beam interacts with a standing wave formed by the reflections from the tapered sections. In the latter case, the gyro-BWO interaction structure can be considered as a cavity. This type of cavity that presents itself as a weakly inhomogeneous waveguide has been analyzed in Ref. [40], and the corresponding complex eigenvalue problem

$$\frac{d^2V}{dz^2}+k_z^2(z)V=0,\qquad(12a)$$

with boundary conditions

$$\frac{dV}{dz}\bigg|_{z=0}jk_zV,\qquad\frac{dV}{dz}\bigg|_{z=L_C}-jk_zV,\qquad(12b)$$

has been formulated. In Eqs. (12), $k_z(z)=[k_l^2-k_c^2(z)]^{1/2}$ means the axial wave number of the waveguide mode, k_l denotes the complex eigennumbers of the cavity modes, $k_c(z)$ means the z dependent cutoff wave number, and L_C denotes the cavity length. The complex eigennumber k_l and the corresponding complex eigenvector V_l determine the eigenfrequency $f_l=\mathrm{Re}\{k_l\}/2\pi$, the quality factor $Q_l=\mathrm{Re}\{k_l\}/2\mathrm{Im}\{k_l\}$, and the field profile $F_l=\|V_l\|$ of the lth eigenmode. Solving Eqs. (12) for the TE_{11} waveguide mode in the interaction structure shown in Fig. 1 results in the eigenfrequency $f_1=33.169$ GHz and the quality factor $Q_1=121$ of the first TE_{111} cavity mode. The field profile F_1 of the TE_{111} cavity mode is presented in Fig. 2(a) by the dashed line.

B. Influence of changing the magnetic field on free-running gyro-BWO operation

As well as in the experiments reported in Ref. [24], in our simulations, an electron beam with the parameters presented in Table I propagates in downstream direction through the structure shown in Fig. 1, which is immersed in a uniform magnetic field B_0. No electron velocity spread is assumed. In this subsection, the results of the simulation of a free-running gyro-BWO operating at different values of the applied magnetic field $1.3\ \mathrm{T}\leqslant B_0\leqslant1.55\ \mathrm{T}$ is presented. In Fig. 3, the calculated upstream P_1 and downstream P_2 output power as well as the operating frequency f_0 are shown. First, changing the applied magnetic field results in tuning the operating frequency over about 1 GHz frequency range and in varying the output power. Second, two distinct jumps both in the upstream output power and in the operating frequency are found, which are related to the changes in the device operating regime. The regions of different operating regimes are marked by the vertical dashed and dash-dotted lines in Fig. 3(b), respectively. These changes are also illustrated in Fig. 2, where field profile F and efficiency versus z coordinate

$$\eta(z)=[\gamma_0-\langle\gamma(z)\rangle]/(\gamma_0-1)\qquad(13)$$

are presented for several values of the magnetic field by solid lines and dots, respectively. In Eq. (13), the subscript 0 denotes values taken at $z=0$ and $\langle\rangle$ means averaging over particles that have entered the interaction structure at the same time. The function $\eta(z)$ demonstrates the process of energy exchange along the axis. If $\eta(z)$ increases, then the electrons give up their energy and vice versa.

At lower magnetic fields $1.32\ \mathrm{T}\leqslant B_0<1.38\ \mathrm{T}$, the device demonstrates stable operation in the gyromonotron regime, radiating in both directions, so that P_1 and P_2 are almost equal to each other. In Fig. 2(a), efficiency $\eta(z)$ and field
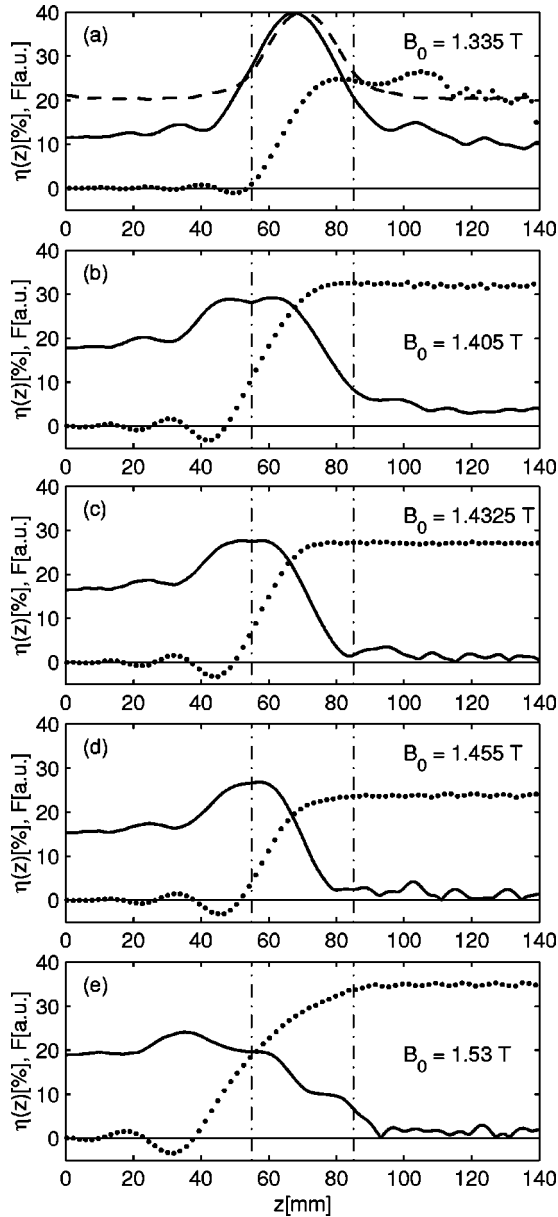
FIG. 2. Efficiency $\eta(z)$ (•) and field profile (solid line) for different values of the applied magnetic field. Vertical dash-dotted lines mark the uniform section ends. In (a), the dashed line represents the field profile of the TE_{111} cold cavity mode.
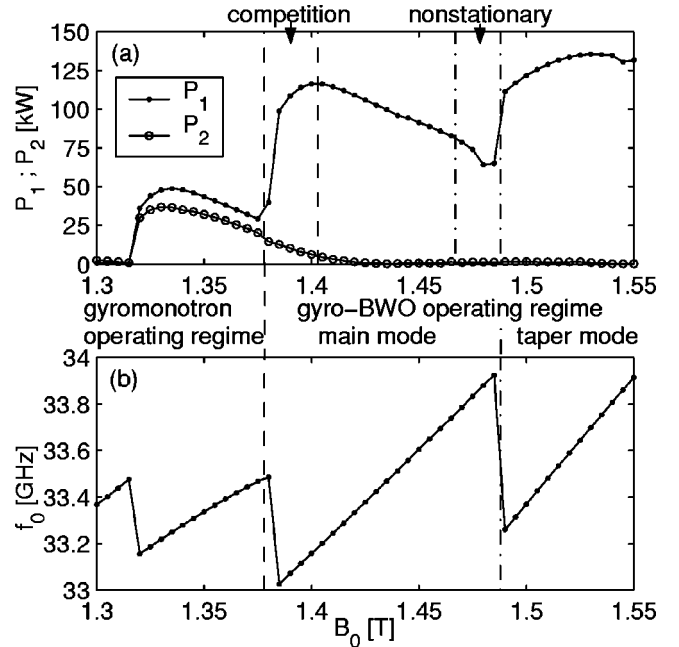

FIG. 3. Upstream P_1 and downstream P_2 output power (a) and operating frequency f_0 (b) of a free-running gyro-BWO vs external magnetic field B_0.

profile are presented for a magnetic field of $B_0 = 1.335$ T, which corresponds to the maximal efficiency in the gyromonotron regime. For comparison, the field profile of the cold cavity mode calculated in the preceding subsection is also presented, showing, on the one hand, a similar form and, on the other hand, the influence of the interaction with an

TABLE I. Electron beam parameters.

Beam voltage	$U_b = 100$ kV
Beam current	$I_b = 4$ A
Beam radius	$R_b = 0.9$ mm
Pitch factor	$\alpha = 1$

electron beam: slight asymmetry and lower amplitude of the field in the tapered sections. Furthermore, function $\eta(z)$ shows how the electrons interact with the electromagnetic field as they pass along the interaction structure. First, this quantity increases and decreases several times in the down-tapered input section where the process of electron bunching in the field of an oppositely propagating traveling wave takes place. Then, the electrons give their energy to the field of a standing wave formed by the reflections from the ends of the central uniform section, which are marked by two vertical dash-dotted lines in Fig. 2. It is worth mentioning that this is different from the case of a conventional gyromonotron cavity, which shows an uptapered input section where no field is present and, therefore, both the electron bunching and the extraction of the energy from the electron beam take place in the field of a standing wave formed in the central uniform section.

After the applied magnetic field becomes higher than 1.38 T, the gyro-BWO interaction comes into play, resulting in a competition between two regimes of operation: a gyromonotron one and a gyro-BWO one. The transient process illustrating this competition for a magnetic field of $B_0 = 1.3825$ T is presented in Fig. 4, where up- and downstream output power and instantaneous operating frequency are shown in (a) and (b), respectively. At the beginning, the device operates in the gyromonotron regime at higher frequency and with approximately equivalent levels of the up- and downstream output power. After a certain time interval, however, an operation in the gyro-BWO regime starts, which leads to competition of two regimes accompanied by frequency and output power modulations. Finally, after about 70 ns, the gyro-BWO operating regime wins the competition and the device starts to operate at a single frequency. The
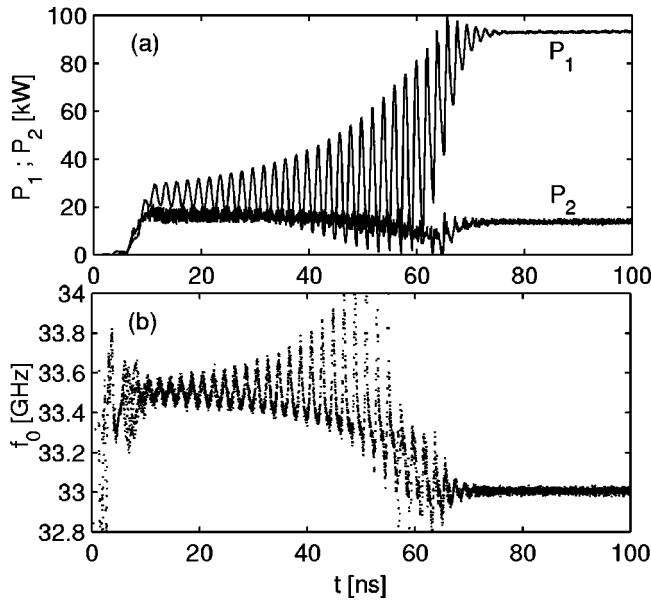
FIG. 4. Transients of upstream P_1 and downstream P_2 output power (a) and instantaneous operating frequency f_0 (b) are depicted for magnetic field $B_0 = 1.3825$ T.

FIG. 5. Output power vs time (a) and spectrum of the corresponding output signal (b) for magnetic field $B_0 = 1.485$ T.

range of magnetic field values corresponding to the competition range is marked by two vertical dashed lines in Fig. 3(a). Over this range, the duration of the transient, which is about 200 ns for $B_0 = 1.38$ T, decreases with increasing magnetic field, so that the transient disappears at $B_0 = 1.405$ T. A further increase in the magnetic field results in tuning the operating frequency and in a reduction of the efficiency. Figures. 2(b)–2(d) demonstrate how efficiency $\eta(z)$ and field profile of the gyro-BWO evolve with increasing magnetic field. The field profile keeps its form showing a profile of a certain axial mode, which will be called the main mode later on. The maximum of the field of the main mode is located in the central uniform section in the vicinity of its upstream end.

Up to $B_0 = 1.465$ T, the gyro-BWO demonstrates stationary operation, afterwards, however, it behaves nonstationary in the following range of magnetic field: 1.465 T $< B_0 < 1.49$ T, which is marked by two vertical dash-dotted lines in Fig. 3(a). The nonstationary regime, which is caused by an excitation of another axial mode, is illustrated in Fig. 5, where output power (a) and spectrum of the corresponding output signal (b) are presented for $B_0 = 1.485$ T. The nonstationary operation not only leads to an appearance of unwanted additional frequency terms in the spectrum but also to a noticeable reduction of the output power. The situation changes when the magnetic field becomes $B_0 \geqslant 1.49$ T. Then the gyro-BWO again shows stationary operation, however, at that axial mode whose excitation at the lower magnetic field value causes the nonstationary operation. Field profile and efficiency $\eta(z)$ of this mode are presented in Fig. 2(e). A comparison of Figs. 2(d) and 2(e) demonstrates the difference between the main mode and its competitor both in the electromagnetic field structure and in the beam-field interaction. Although, for the main mode, extraction of the energy from the electrons takes place mainly in the uniform section,
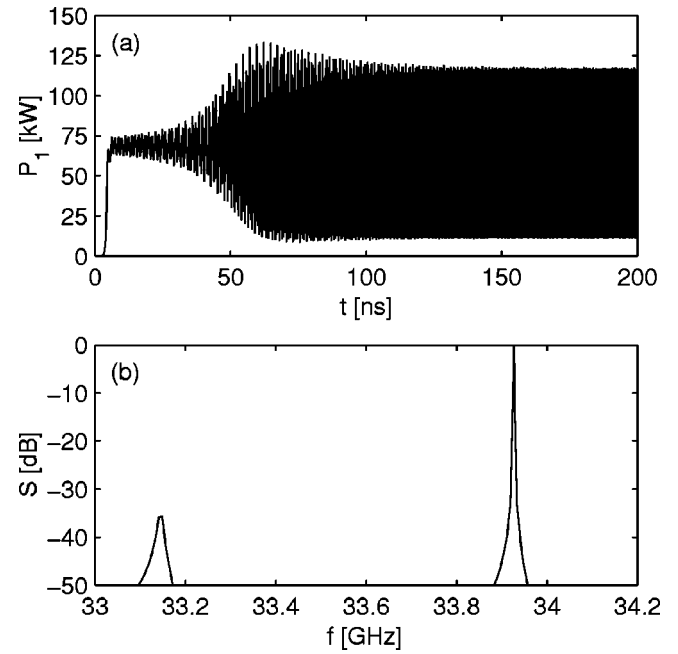
the other mode extracts the energy both in the downtapered input section and in the uniform section. In the opposite, the region of electron bunching becomes shorter than that for the main mode. Moreover, the maximum of the field of the latter mode is located in the downtapered input section. Hence, this mode will be called taper mode. Although the efficiency of operation in the taper mode is higher than that in the main mode, the frequency tuning curve, which is presented in Fig. 3(b) shows a second jump to lower frequencies demonstrating the limitation, which is imposed on the frequency tuning bandwidth by the excitation of the parasitic taper mode.

C. Self-consistent Q-factor and Adler's relation

In the gyromonotron regime, the noticeable difference between the cold cavity field profile and that one calculated self-consistently taking into account the electron beam (both presented in Fig. 2(a) by the dashed and by the solid lines, respectively) results in a substantial difference in the corresponding Q factors: the Q factor of the cold cavity and the Q factor of the cavity in the presence of the electron beam. Using the results of the self-consistent simulations, the latter one can be calculated from the general definition: $Q = 2\pi f_0 W / P_0$, where $P_0 = P_1 + P_2$ means output power and W denotes average stored electromagnetic energy. This calculation can be performed not only for the gyromonotron operating regime, where we can speak about interaction with a cavity mode, but also for the gyro-BWO regime, where the electrons interact with a traveling wave. In Table II, f_0, P_0, and the self-consistently calculated Q are presented for those values of the applied magnetic field that have been used in Fig. 2. For $B_0 = 1.335$ T, the self-consistent $Q = 366$ is about three times higher than that of the cold cavity $Q_1 = 121$ calculated in Sec. III A. Such a large relative increase is not

TABLE II. Operating frequency f_0, output power P_0, and self-consistent quality factor Q of free-running gyro-BWO for different values of magnetic field B_0 corresponding to Fig. 2.

B_0 (T)	f_0 (GHz)	P_0 (kW)	Q
1.335	33.246	83	366
1.405	33.202	121	226
1.4325	33.446	102	210
1.455	33.651	89	206
1.53	33.699	136	159

typical for gyromonotron cavities. For example, in the injection-locked gyromonotron experiments reported in Ref. [34], a much smaller increase from 450 up to 510 has been observed. A possible explanation is the smaller value of Q_1 compared to the typical Q factor of gyromonotron cavities, which results in a lower stability of the cold cavity field profile against an influence of the electron beam. The data from Table II will be used in the following two subsections to estimate a locking bandwidth Δf_L both in gyromonotron and in gyro-BWO operating regimes according to the well-known Adler's relation derived in Ref. [26], which is given by

$$\Delta f_L = \frac{f_0}{Q}\left(\frac{P_{inj}}{P_0}\right)^{1/2} \tag{14}$$

and proves to be valid for a very broad class of oscillators including gyromonotrons locked by an external signal, which is injected directly into the cavity (see Refs. [34–36]).

D. Injection-locked operation of gyro-BWO

In this section, the results of the numerical study of injection locking of the gyro-BWO, which was investigated in the preceding subsections, are presented. In order to distinguish locked and unlocked states of operation, a fast Fourier transform (FFT) of the output signal calculated up to $t_{max} = 200$ ns is analyzed. In this case, the frequency resolution is $df = 1/(2t_{max}) = 2.5$ MHz. Moreover, visual examination of the output power versus time dependence allows the frequency resolution in differentiating locked and unlocked states to be improved by a factor of 2.

In Fig. 6, the results of simulations of the gyro-BWO operating in the presence of an external signal, which is injected through the upstream port, as in the experiments reported in Ref. [24], are shown for different values of the applied magnetic field B_0, which correspond to Fig. 2. In the plane of parameters P_{inj} (power of injected signal) and f_{inj} (frequency of injection signal), the dots (•) correspond to locked operation of the gyro-BWO, whereas the crosses (×) denote unlocked states. The borders of the locked operation region, where the dots are located, represent the locking bandwidth curve. For a very small injection signal ($P_{inj}/P_0 < -30$ dB), the frequency resolution seems to be not sufficient to accurately determine the locking bandwidth curve. Nevertheless, these data are also presented. The locking bandwidth curves calculated from Adler's relation (14)
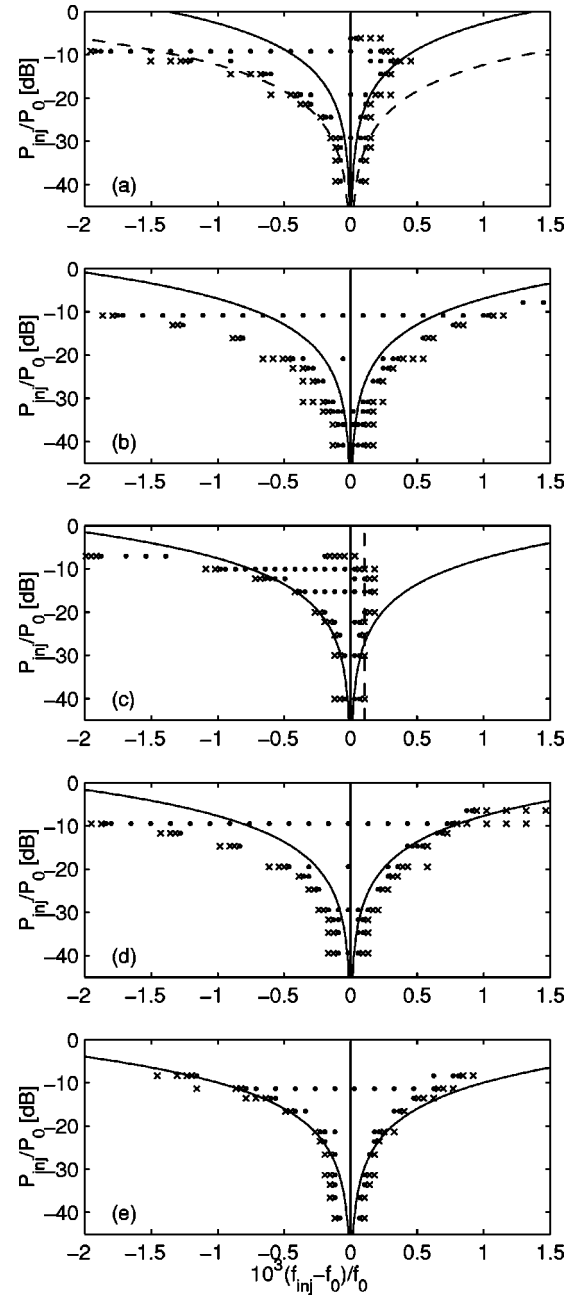

FIG. 6. Locked (•) and unlocked (×) operation states are depicted in the plane P_{inj} vs f_{inj} for different values of magnetic field B_0 corresponding to Fig. 2. The solid lines show the locking bandwidth Δf_L calculated using the parameters from Table II. The upstream port is used for injection.

using the parameters of the free-running gyro-BWO presented in Table II are also shown for comparison by the solid lines. Moreover, in Fig. 6(a), the dashed line shows the locking bandwidth curve for the Q_1 value of the cold cavity mode calculated in Sec. III A.

The locking bandwidth curves from Figs. 6(b) and 6(d), which correspond to magnetic field values $B_0 = 1.405$ T and 1.455 T, respectively, are very close to the experimental results reported in Ref. [24], which have been obtained for slightly higher values of the magnetic field, demonstrating a

good quantitative agreement. Both the locking bandwidth and the asymmetry of the locking bandwidth curves with respect to the free-running frequency f_0 well agree. However, for an intermediate value of magnetic field $B_0 = 1.4325$ T, the numerical results presented in Fig. 6(c) are quite different from both the results of the simulation shown in Figs. 6(b) and 6(d) and the experimental results. The locking bandwidth is about 2.5 times smaller. This significant difference demonstrates the influence of changing the applied magnetic field on the locking bandwidth of the gyro-BWO. Moreover, an interesting phenomenon is observed, namely, that the right branch of the locking bandwidth curve is not unique but double valued. Consequently, for some injection frequencies, the gyro-BWO is only locked in a limited range of P_{inj} (for example, for $f_{inj} = 33.45$ GHz, which is marked in Fig. 6(c) by the vertical dashed line, this range is 0.3 kW$<P_{inj}<$10 kW). Furthermore, injecting the signal at the free-running frequency with power, which is above some threshold level (for the case presented in Fig. 6(c), this level is in between 10 and 20 kW) leads to unlocked operation of the gyro-BWO. In all the three cases presented in Figs. 6(b)–6(d), the gyro-BWO operates in the main mode and the corresponding field profile and efficiency $\eta(z)$, which are shown in Figs. 2(b)–2(d) look very similar to each other. Hence, such a strong variation of locking bandwidth with varying magnetic field is unexpected. Another question is why the locking bandwidth curves are asymmetric.

To proceed further, the locking bandwidth curve of the gyro-BWO has been calculated in the gyromonotron operating regime at $B_0 = 1.335$ T and for operation in the taper mode at $B_0 = 1.53$ T. The results are presented in Figs. 6(a) and 6(e), respectively. Both are of great help at least in answering the question about asymmetry. Indeed, according to the experimental data presented in Refs. [34,35], conventional gyromonotrons with uptapered input section where the external signal is injected into the downstream port demonstrate symmetrical locking bandwidth curves. In opposite, the locking bandwidth curve of the gyro-BWO operating in the gyromonotron regime, which is presented in Fig. 6(a), is even more asymmetric than the locking bandwidth curves of the gyro-BWO operating in the main mode. The reason for that obviously is the injection of the external signal into the upstream port. In this case, the injection signal propagates in downstream direction through the downtapered input section where electron bunching occurs over a relatively long distance both in the gyromonotron and in the main mode gyro-BWO regime [see Figs. 2(a) and 2(b)–2(d), respectively]. On the other side, the locking bandwidth curve of the gyro-BWO operating in the taper mode, which is shown in Fig. 6(e), demonstrates only slight asymmetry compared to Figs. 6(a)–2(d) what is consistent with the above supposition because the gyro-BWO operating in the taper mode shows shorter bunching length compared to the gyro-BWO operating in the main mode [compare Fig. 2(a)–2(d) and 2(e)] and is less affected by the injection signal. To check our supposition, the injection-locking of the gyro-BWO from the downstream port has numerically been investigated. The results are presented in Fig. 7 demonstrating no asymmetry in the locking bandwidth curves of the gyro-BWO operating in
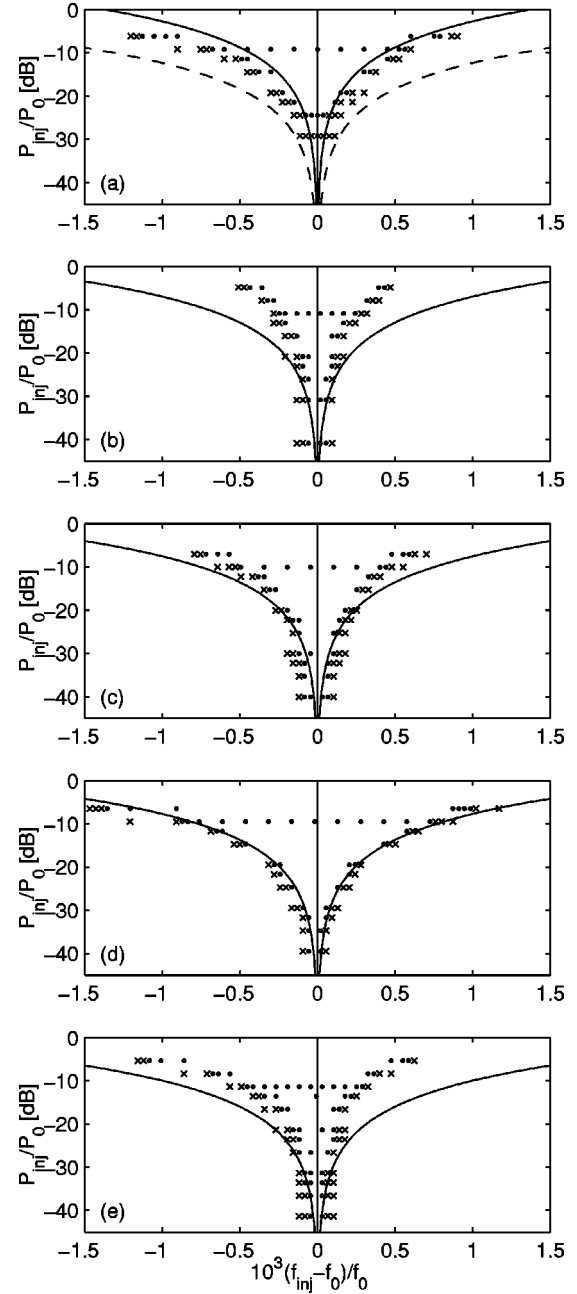

FIG. 7. The same as Fig. 6 but the downstream port is used for injection.

the gyromonotron regime and in the main mode gyro-BWO regime and thus confirming our supposition.

To speak also in terms of numbers, in addition to the locking bandwidth $\Delta f_L^{(i)} = f_{inj}^+ - f_{inj}^-$, where f_{inj}^- and f_{inj}^+ denote two frequencies limiting the locking band at a certain value of injection power P_{inj} from left and right, respectively, the mismatch between the central frequency of the locking band and the free-running frequency f_0 defined as $\Delta f_0^{(i)} = (f_{inj}^+ + f_{inj}^-)/2 - f_0$ is introduced in order to quantify the asymmetry of locking bandwidth curves. The corresponding numerical values of the locking bandwidth $\Delta f_L^{(i)}$ and the mismatch $\Delta f_0^{(i)}$ are presented in Table III for $P_{inj}/P_0 = -10$ dB. First, in terms of numbers, it is even

TABLE III. Locking bandwidth $\Delta f_L^{(i)}$ and mismatch $\Delta f_0^{(i)}$ for injection into the upstream ($i=1$) and into the downstream ($i=2$) ports, along with the locking bandwidth Δf_L calculated using the parameters from Table II for an injection power of $P_{inj} = 0.1 P_0$.

B_0 (T)	$\Delta f_L^{(1)}$ (MHz)	$\Delta f_0^{(1)}$ (MHz)	$\Delta f_L^{(2)}$ (MHz)	$\Delta f_0^{(2)}$ (MHz)	Δf_L (MHz)
1.335	63	-23	38	-1	29
1.405	103	-13	20	0	47
1.4325	34	-16	30	-1	50
1.455	81	-15	51	-2	52
1.53	56	-4	31	-4	67

more pronounced that the strong asymmetry of the locking bandwidth curves in the first four cases is due to the influence of the injection signal on the process of electron bunching in the downtapered input section, but that it is not a feature of the gyro-BWO type of interaction. Moreover, the factor of about $\sqrt{2}$ between $\Delta f_0^{(1)} = -23$ MHz for $B_0 = 1.335$ T, which corresponds to the gyromonotron regime, and $\Delta f_0^{(1)} = -(13+16+15)/3 \approx -15$ MHz for $B_0 = \{1.405, 1.4325, 1.455\}$ T, which corresponds to the main mode gyro-BWO regime, is because, in the gyromonotron regime, the output power propagates through both apertures and, therefore, the amplitude of the electric field in the tapered sections is $\sqrt{2}$ times lower compared to that in the gyro-BWO regime for the same output power level. Second, for $B_0 = 1.53$ T corresponding to the operation in the taper mode gyro-BWO regime, the slight asymmetry is not influenced by the presence of the injection signal in the downtapered input section that indicates its different nature. Third, the increase of the locking bandwidth in four from five cases must also be attributed to the influence of the external signal, injected into the upstream port, on the electron bunching. This also agrees with the experimental results on the locked gyromonotron where an electron beam has been modulated by an external signal in a prebunching cavity and by ballistic bunching in the drift region between the prebunching and the main cavities. In this experiment, a factor of 10 increase in the locking bandwidth, compared to the direct injection locking, has been reported in Ref. [35]. In our case, the largest increase in the locking bandwidth is about five times for $B_0 = 1.405$ T, which corresponds to the operation in the main gyro-BWO mode at the maximum of the free-running efficiency. Fourth, Adler's relation gives correct value of the locking bandwidth only in the case of operation in the gyromonotron regime and injection into the downstream port that agrees with the previous experimental and numerical results. In the other cases, it gives only an approximate value that can differ by several times from the correct locking bandwidth.

E. Influence of injection-locking on gyro-BWO output power

In the experiments reported in Ref. [24], a significant increase in the locked output power compared to the free-running output power P_0 has been observed. This has moti-
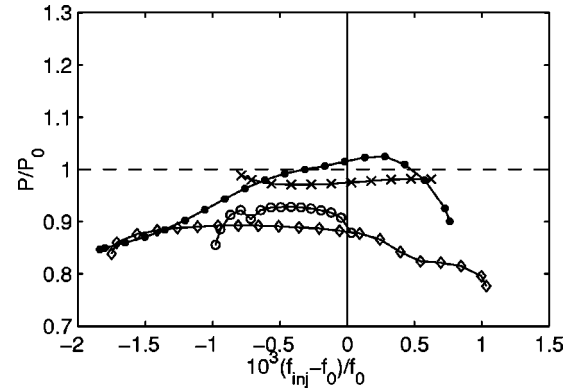

FIG. 8. Output power of locked gyro-BWO normalized to the corresponding power of free-running gyro-BWO vs injection frequency for different values of magnetic field B_0: 1.405 T ($\diamond$), 1.4325 T ($\bigcirc$), 1.455 T ($\bullet$), and 1.53 T ($\times$). Injection power $P_{inj} = 10$ kW. The upstream port is used for injection.

vated us to investigate the locked output power versus injection frequency dependence for fixed value of injection power $P_{inj} = 10$ kW. In Fig. 8, the results of this investigation are presented for injection into the upstream port and for different values of the magnetic field corresponding to an operation in the gyro-BWO regime. Only one curve for $B_0 = 1.455$ T, which is shown by dots and which corresponds to the lowest free-running output power demonstrates a relative increase in the locked output power of about 2% at an injection frequency slightly higher than the free-running frequency. This is in agreement with the experimental results for an operating point far from the maximum value of the free-running output power where about 10% increase in the locked output power has been found. However, the significant increase of about 50% in the locked output power over the free-running output power, which has been observed in the experiment for an operating point close to the maximum value of the free-running output power, is not found in the simulations. In fact, a decrease in the locked output power compared to the free-running output power is found in the simulation for $B_0 = 1.405$ T, which corresponds to the operation at the maximum of the free-running output power (see diamonds in Fig. 8).

The curves in Fig. 8 are rather different from each other, which is caused by the presence of the injection signal in the downtapered input section. To see the effect of this influence on the power enhancement by the injection-locking, injection into the downstream port is also investigated. The results are presented in Fig. 9. All parameters are the same as in Fig. 8 but the signal is injected into the downstream port. All curves show similar shape which is also similar to the shape of the curves presented in Ref. [29] where a gyromonotron synchronization has been investigated numerically. The same scale is used in both Figs. 8 and 9, in order to demonstrate the difference between the curves in these two figures resulting from the influence of the injection signal on electron bunching, which takes place in the downtapered input section. All four curves in Fig. 9 demonstrate a locked power increase but by different amounts. Whereas for $B_0 = 1.405$ T corresponding to the maximum value of the free-
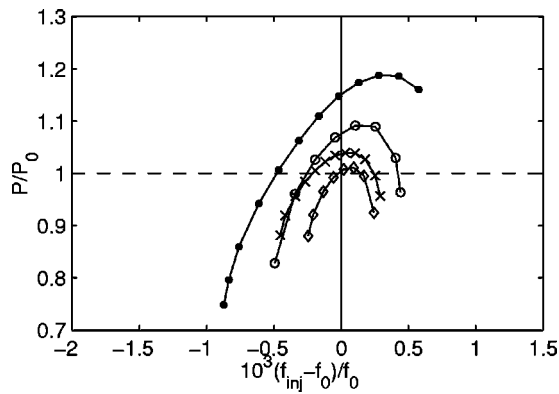
FIG. 9. The same as Fig. 8 but the downstream port is used for injection.

running output power, the increase is only about 1%, resulting in a locked output power of about 123 kW, the increase for $B_0 = 1.455$ T corresponding to the lowest value of the free-running output power is 20%. This is the maximum increase observed in the simulations, resulting in a locked output power of about 107 kW, which has again been obtained at an injection frequency, which is slightly higher than the free-running frequency. Hence the experimentally observed increase in the locked power of about 50% over the free-running power, which has been reported in Ref. [24], is not found in the simulations. This disagreement can be attributed to the influence of the electromagnetic fields in the region of the upstream input coupler on the electron bunching, which is not taken into account in the simulations.

IV. CONCLUSIONS

The presented numerical results reveal important details of the injection-locked operation of a gyro-BWO with tapered sections and its dependence on the applied magnetic field. In the free-running operating regime, increasing the magnetic field leads to an operating frequency jump due to the excitation of an undesired taper mode, which reduces the magnetic tuning bandwidth to 1 GHz for the cases considered. Moreover, nonstationary behavior caused by the coexistence of the main and the taper mode has been observed in a certain range of the magnetic field values. In the injection-locked gyro-BWO, significant modifications of the locking bandwidth curve have been observed if the magnetic field is tuned for the case of injection into the upstream port. In two cases, the locking bandwidth curves that have been found in the simulations as well as their asymmetry agree with the experiments. In one case, the locking bandwidth curve shows a complicated form, which is probably difficult to determine experimentally. Comparison of these results to the results for an operation in the gyromonotron regime and further to the results for injection into the downstream port leads to the following conclusions. The asymmetry of the locking bandwidth curves, which has been found in the case of injecting into the upstream port both in the gyro-BWO and in gyromonotron regimes, is caused by the influence of the injection signal on the electron bunching, which takes place in the downtapered input section. This is also the reason for an increase of the locking bandwidth, which could be observed in four out of five cases that have been investigated. The largest increase, which is a factor of 5, has been found at a magnetic field value corresponding to an operation in the main gyro-BWO mode at the maximum value of the output power. Adler's relation has been found to be accurate only in the gyromonotron regime for injection into the downstream port, which agrees well with previous results. In the other cases, it can give only approximate estimates that are, however, also very useful. The increase in the locked output power over the free-running output power has been found to be in agreement with the experimental results for operation far from the operation that leads to a maximum of the free-running output power (i.e., far from the cutoff frequency of the central uniform section). The increase is higher for the case of injection into the downstream port compared to the case of injection into the upstream port. The highest increase that has been found in the simulations is 20%. The significant increase of about 50% of the locked output power over the free-running output power, which has been observed experimentally in Ref. [24] when operating close to the maximum of the efficiency (i.e., close to the cutoff frequency of the central uniform section), has not been found in the simulations.

[1] G.S. Nusinovich and O. Dumbrajs, IEEE Trans. Plasma Sci. **24**, 620 (1996).

[2] N.S. Ginzburg, I.G. Zarnitsyna, and G.S. Nusinovich, Radio Eng. Electron. Phys. **24**, 113 (1979).

[3] J.M. Wachtel and E.J. Wachtel, Appl. Phys. Lett. **37**, 1059 (1980).

[4] S.Y. Park, V.L. Granatstein, and R.K. Parker, Int. J. Electron. **57**, 1109 (1984).

[5] A.K. Ganguly and S. Ahn, Int. J. Electron. **67**, 261 (1989).

[6] A.Y. Dmitriev, D.I. Trubetskov, and A.P. Chetverikov, Radiophys. Quantum Electron. **34**, 502 (1991).

[7] A.T. Lin and P.K. Kaw, Int. J. Electron. **72**, 887 (1992).

[8] A.T. Lin, Phys. Rev. A **46**, R4516 (1992).

[9] A.T. Lin and C.-C. Lin, Phys. Fluids **5**, 2314 (1993).

[10] C.S. Kou, Phys. Fluids **1**, 3093 (1994).

[11] C.S. Kou, C.H. Chen, and T.J. Wu, Phys. Rev. E **57**, 7162 (1998).

[12] S.H. Chen, K.R. Chu, and T.H. Chang, Phys. Rev. Lett. **85**, 2633 (2000).

[13] G.S. Nusinovich, A.N. Vlasov, and T.M. Antonsen, Jr., Phys. Rev. Lett. **87**, 218301 (2001).

[14] A. Grudiev and K. Schünemann, IEEE Trans. Plasma Sci. **30**,

851 (2002).

[15] S.H. Chen, K.F. Pao, T.H. Chang, C.T. Fan, and K.R. Chu, in *Digest of 27th International Conference on Infrared and Millimeter Waves*, edited by R. J. Temkin (IEEE, San Diego, CA, 2002), pp. 333 and 334.

[16] S.Y. Park, R.H. Kyser, C.M. Armstrong, R.K. Parker, and V.L. Granatstein, IEEE Trans. Plasma Sci. **18**, 321 (1990).

[17] T.A. Spencer, R.M. Gilgenbach, and J.J. Choi, J. Appl. Phys. **72**, 1221 (1992).

[18] C.S. Kou, S.H. Chen, L.R. Barnett, H.Y. Chen, and K.R. Chu, Phys. Rev. Lett. **70**, 924 (1993).

[19] M.T. Walter, R.M. Gilgenbach, P.R. Menge, and T.A. Spencer, IEEE Trans. Plasma Sci. **22**, 578 (1994).

[20] M.A. Basten, W.C. Guss, K.E. Kreischer, R.T. Temkin, and M. Caplan, Int. J. Infrared Millim. Waves **16**, 889 (1995).

[21] M.T. Walter, R.M. Gildenbach, J.W. Luginsland, J.M. Hochman, J.I. Rintamaki, R.L. Jaynes, Y.Y. Lau, and T.A. Spencer, IEEE Trans. Plasma Sci. **24**, 636 (1996).

[22] T.A. Spencer, C.E. Davis, K.J. Hendricks, F.J. Agee, and R.M. Gildenbach, IEEE Trans. Plasma Sci. **24**, 630 (1996).

[23] K. Kamada, K. Nawashiro, F. Tamagawa, H. Igarashi, S. Kizu, C.-Y. Lee, S. Kawasaki, R. Ando, and M. Masuzaki, Int. J. Infrared Millim. Waves **19**, 1317 (1998).

[24] T.H. Chang, S.H. Chen, F.H. Cheng, C.S. Kou, and K.R. Chu, in *Digest of 24th International Conference on Infrared and Millimeter Waves*, edited by L. A. Lombardo (University of California, Davis, Monterey, CA, 1999), pp. M–A2.

[25] T.H. Chang, S.H. Chen, L.R. Barnett, and K.R. Chu, Phys. Rev. Lett. **87**, 064802 (2001).

[26] R. Adler, Proc. IRE **34**, 351 (1946).

[27] A. Pikovsky, M. Rosenblum, and J. Kurths, *Synchronization: A Universal Concept in Nonlinear Sciences* (Cambridge University Press, Cambridge, 2001).

[28] V.S. Ergakov and M.A. Moiseev, Radiophys. Quantum Electron. **18**, 89 (1975).

[29] V.S. Ergakov, M.A. Moiseev, and V.I. Khyzhnyak, Radio Eng. Electron. Phys. **23**, 92 (1978).

[30] A.W. Fliflet and W.M. Manheimer, Phys. Rev. A **39**, 3432 (1989).

[31] P.E. Latham, V.L. Granatstein, and Y. Carmel, Int. J. Infrared Millim. Waves **14**, 1217 (1993).

[32] P.E. Latham, B. Levush, G.S. Nusinovich, and S. Parikh, IEEE Trans. Plasma Sci. **22**, 818 (1994).

[33] J. Jelonnek and K. Schünemann, in *Digest of 22'st International Conference on Infrared and Millimeter Waves*, edited by H. P. Freund (IEEE, Wintergreen, VA, 1997), pp. 293 and 294.

[34] M.E. Read, R. Seeley, and W.M. Manheimer, IEEE Trans. Plasma Sci. **13**, 398 (1985).

[35] A.H. McCurdy, C.A. Armstrong, W.M. Bollen, R.K. Parker, and V.L. Granatstein, Phys. Rev. Lett. **57**, 2379 (1986).

[36] H. Guo *et al.*, IEEE Trans. Plasma Sci. **23**, 822 (1995).

[37] J. Jelonnek, A. Grudiev, and K. Schünemann, IEEE Trans. Plasma Sci. **27**, 374 (1999).

[38] A. Grudiev, J. Jelonnek, and K. Schünemann, Phys. Plasmas **8**, 2963 (2001).

[39] R.F. Harrington, *Time-Harmonic Electromagnetic Fields* (McGraw-Hill, New York, 1961).

[40] S.N. Vlasov, G.M. Zhislin, I.M. Orlova, M.I. Petelin, and G.G. Rogacheva, Radiophys. Quantum Electron. **12**, 972 (1969).